ADVANCED FUNCTIONAL MATERIALS
www.afm-journal.de

Materials Views
www.MaterialsViews.com

From Bonding Asymmetry to Anharmonic Rattling in $Cu_{12}Sb_4S_{13}$ Tetrahedrites: When Lone-Pair Electrons Are Not So Lonely

Wei Lai, Yuxing Wang, Donald T. Morelli, and Xu Lu*

Some of the best thermoelectrics are complex materials with rattling guests inside oversized atomic cages. Understanding the chemical and structural origins of the rattling behavior is essential to the design of thermoelectric materials. In this work, a clear connection is established between the local bonding asymmetry and anharmonic rattling modes in tetrahedrite thermoelectrics, enabled by the chemically active electron lone pairs. The studies reveal a five-atom atomic cage Sb[CuS_3]Sb in $Cu_{12}Sb_4S_{13}$ tetrahedrites that exhibits strong local bonding asymmetry: covalent bonding inside the CuS_3 trigonal plane and weak out-of-plane bonding induced by the lone-pair electrons of Sb. This bonding asymmetry leads to out-of-plane rattling modes that are quasilocalized and anharmonic with low frequency and large amplitude, and are likely the origin of low thermal conductivity in tetrahedrites. Such knowledge highlights the importance of local structure asymmetry and lone-pair atoms in driving anharmonic rattling, providing a stepping stone to the discovery and design of next-generation thermoelectrics.

1. Introduction

Thermoelectric devices enable direct conversion between thermal energy and electrical energy and hold great potential in solid-state waste heat recovery and cooling applications.[1] The performance of thermoelectric materials is controlled by both thermal and electrical properties and is quantified collectively by a dimensionless figure of merit $zT = S^2\sigma T/\kappa$, where S is the Seebeck coefficient, σ is the electrical conductivity, and T is the absolute temperature. The thermal conductivity κ includes both the electronic κ_e and lattice contributions κ_L as $\kappa = \kappa_e + \kappa_L$. The electrical and thermal conductivities of electrons are correlated by the Wiedemann–Franz law. Thus to achieve high zT values, it is desirable to increase the electrical conductivity σ while decreasing the lattice thermal conductivity κ_L. Such a concept has been coined by Slack as phonon glass/electron crystal (PGEC).[2]

One strategy to achieve PGEC in a material is to adopt a guest–framework/host structure, in which the framework is electrically conducting while the guest reduces the lattice thermal conductivity. Such a guest atom has been termed by Slack and Tsoukala[3] as a rattling atom or a rattler. It was proposed that these rattlers scatter the heat-carrying acoustic phonons to decrease the lattice thermal conductivity. To accommodate rattlers, it is reasonable to look for cage compounds with oversized atomic cages such as clathrates and partially filled skutterudites. For example, in $Ba_8Ga_{16}Ge_{30}$ clathrates, the oversized atomic cages are tetrakaidecahedra (24 atom) made of Ga and Ge atoms while a single Ba atom inside the cage behaves as a rattler.[4] In $M_xCo_4Sb_{12}$ (M is a metal atom) skutterudites, the oversized atomic cages are icosahedra (12 atom) made of Sb atoms while a single M atom behaves as a rattler.[5]

Recently, tetrahedrites based on the $Cu_{12}Sb_4S_{13}$ composition with earth-abundant and environmentally friendly elements were discovered to be promising thermoelectric materials. For example, Lu et al.[6] reported zT values in excess of unity at 700 K for $Cu_{12}Sb_4S_{13}$ codoped with Zn and Ni. Furthermore, lattice thermal conductivity values of many compositions in this family are close to or below 0.5 W K^{-1} m^{-1} from 300 to 700 K.[6,7] Such a small value is generally only found in amorphous solids in which the phonon mean free path is close to the interatomic spacing, i.e., so-called minimum thermal conductivity (MTC) by Slack.[8]

The crystallographic structure of $Cu_{12}Sb_4S_{13}$ has been known for decades since the early work of Wuensch.[9] The space group is I-43m and features two Cu sites (12d and 12e), two S sites (2a and 24g), and one Sb site (8c). Cu12e site is associated with large atomic displacement parameters (ADPs) even at ambient temperature. Thus it was proposed that Cu12e atoms behave as rattlers in $Cu_{12}Sb_4S_{13}$ based tetrahedrites.[7a,b] However, in contrast to clathrates and filled skutterudites, no oversized atomic cages have been identified in tetrahedrites. To understand MTC in similar compounds such as Cu_3SbSe_4, $CuSbSe_2$, and Cu_3SbSe_3, Skoug and Morelli[10] focused on the influence of electron lone pairs of Sb and suggested that the electrostatic repulsion between Sb lone pairs and neighboring Se atoms creates the anharmonicity in the lattice and hence

Prof. W. Lai, Dr. Y. Wang, Prof. D. T. Morelli, Dr. X. Lu
Department of Chemical Engineering
and Materials Science
Michigan State University
East Lansing, MI 48824, USA
E-mail: laiwei@msu.edu

DOI: 10.1002/adfm.201500766

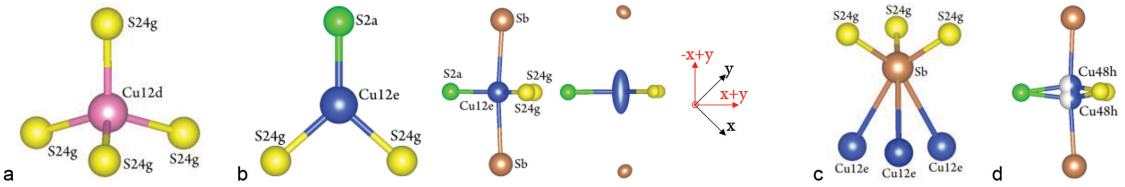

Figure 1. Representative structure units in the a–c) "average0" and d) "average1" structures of $Cu_{12}Sb_4S_{13}$. a) A CuS_4 tetrahedron with Cu12d and S24g. b) A Sb[CuS_3]Sb trigonal bipyramid: S2a and S24g atoms around Cu12e atom in the triangular plane; side view of the plane with Sb atoms above and below; atomic displacement in the form of ellipsoids (90% probability); relation between the original (x, y, z) and new coordinate ($x+y$, $-x+y$, z) system. The local lattice vectors of the new coordinate system will be named as 1′, 2′, and 3′. c) A S_3SbCu_3 trigonal antiprism with Sb, S24g, and Cu12e atoms. d) Off-center/out-of-plane Cu atoms in the split-site "average1" model. The same color code, i.e., pink for Cu12d, blue for Cu12e/Cu48h, green for S2a, yellow for S24g, and brown for Sb, is used throughout this work.

the MTC. In $Cu_{12}Sb_4S_{13}$ tetrahedrites, it has been hypothesized that Sb lone pairs have a similar influence. However, such an argument implies that the lone pairs are only sterically or stereochemically active,[11] consistent with the valence shell electron pair repulsion theory. The exact chemical nature of interaction between the Sb lone pairs and other lattice atoms and its contribution to rattling remain elusive. For example, is the chemical bonding between Sb and Cu12e ionic or covalent? Do Sb lone pairs participate directly in the bonding? What is the direct connection between Sb lone pairs and rattling/anharmonicity?

The objective of the present work is to obtain atomic insight into chemical bonding and atomic dynamics in the prototypical tetrahedrite $Cu_{12}Sb_4S_{13}$. We study the chemical bonding by employing real-space descriptors such as atomic charge, bond order (BO), and electron localization function[12] (ELF) to quantify the ionicity, covalency, and lone pair bonding capability of various atomic pairs (especially Cu12e–Sb pairs). These descriptors build on the electron charge density computed from the density functional theory (DFT). An atomic charge value of zero indicates pure covalency while a value of formal charge reflects pure ionicity. Similarly, a bond order value of zero indicates pure ionic and a value of one reflects a full single covalent bond. Finally, an ELF value of 0.5 indicates delocalized electron gas while a value of one reflects full localization. The region with high ELF values signifies the position of covalent bonding or electron lone pairs. In addition, we study the atomic dynamics, especially the anharmonic rattling, by employing real-space descriptors such as vibrational density of states (VDOS), mean square displacement (MSD), and atomic probability density function (p.d.f.) on the atomic trajectory from the DFT-based first-principles molecular dynamics (FPMD) simulations. FPMD has the advantage over lattice dynamics in that it naturally incorporates anharmonicity. Electron density and atomic dynamics from the calculation are validated against results from the synchrotron diffraction.

2. Results

2.1. Crystallographic/Average Structure

Based on the commonly accepted crystallographic model of $Cu_{12}Sb_4S_{13}$ from Wuensch[9] and Pfitzner et al.,[13] Rietveld refinement ("RR") results from synchrotron data at 100 and 295 K are presented in Table S1 (Supporting Information). These structural parameters are similar to those from X-ray diffraction of $Cu_{12}Sb_4S_{13}$ single crystals[9,13] and from synchrotron powder diffraction of $Cu_{11}Ni_1Sb_4S_{13}$[7b] at similar temperatures. Such crystallographic structure will be named as "average0" structure for the following discussion. Some representative units in the "average0" structure are shown in **Figure 1**. First, each Cu12d atom forms a tetrahedron with four S24g atoms (Figure 1a). Second, each Cu12e atom forms a triangular planar coordination with one S2a atom and two S24g atoms (Figure 1b). This CuS_3 trigonal plane was treated as a fundamental structure unit in the previous studies.[9,13] However, we will incorporate the two Sb atoms above and below the plane to form a Sb[CuS_3]Sb trigonal bipyramid. The angle of Sb–Cu12e–Sb triplet is ≈175°. Plotting anisotropic ADPs of Cu12e atoms in the form of 90% probability ellipsoids indicates that their displacement is perpendicular to the triangular plane. It is convenient to transform the original coordinate system (x, y) to the new one ($x + y$, $-x + y$) so the elongation of Cu12e is along the $-x + y$ direction. Third, each Sb atom is coordinated with three S24g atoms as an SbS_3 trigonal pyramid (Figure 1c). Again, we will incorporate the Sb–Cu12e pairs to form an S_3SbCu_3 trigonal antiprism. In terms of S coordination, each S2a is coordinated with six Cu12e atoms, while each S24g atom is coordinated with one Sb, one Cu12e, and two Cu12d atoms (not shown).

Noteworthy in Table S1 (Supporting Information) is the unusually large anisotropic ADPs ($U_{2'2'}$ = 0.1091 Å^2) of Cu12e atoms even at 100 K, suggesting possible static/positional (e.g., off-center) disorder that is common in ionic conductors. For example, U_{11} of lithium at 48g site is as large as 0.12 Å^2 at 10 K in lithium garnet oxide $Li_5La_3Ta_2O_{12}$.[14] This was reconciled by a split-site model using a low-symmetry site, i.e., 96h, along the direction of abnormal displacement. In the clathrate thermoelectric $Sr_8Ga_{16}Ge_{30}$, the split-site model was also employed for the Sr2 atom.[15] Enlightened by this approach, here we replace the on-center/in-plane 12e site with off-center 48h site that is out of the triangular plane, as can be visualized in Figure 1d. Two Cu48h atoms are visible due to the symmetry of the site. Rietveld refinement results for this split-site model, called "average1" hereafter, are shown in Table S2 (Supporting Information). We only applied isotropic ADPs for Cu48h sites. The overall quality of the refinement, lattice parameters, atomic coordinates, ADPs of Cu12d, Sb, S2a, and

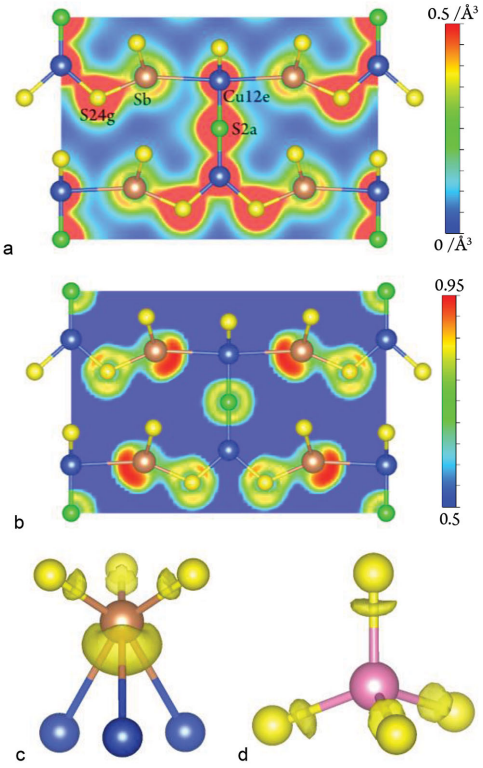

Figure 2. Valence electron density and ELF maps of the "average0" structure. a) Valence electron density map projected onto a (101) plane showing the coordination of Cu12e, Sb, S2a, and S24g atoms. b) ELF map of the same atoms as in (a). c) ELF map of a S_3SbCu_3 trigonal antiprism showing the covalent bonding between Sb and S24g and the electron lone pair of Sb (isosurface level of 0.82). d) ELF map of a CuS_4 tetrahedron showing the covalent bonding between Cu12d and S24g (isosurface level of 0.86).

S24g are almost identical between "average0" and "average1" structures. The isotropic ADPs of Cu48h declined to values of around 0.02–0.03 $Å^2$, comparable to those of Cu12d. The out-of-plane distances of Cu48h are around 0.27 and 0.30 Å at 100 and 295 K, respectively.

2.2. Valence Electron Charge Density and Bonding: Average0

Chemical bonding in materials can be understood from the valence electron charge density resulting from the DFT-based energy minimization. The charge density and ELF maps encompassing the structure units around Cu12e and Sb atoms in the "average0" structure are shown in **Figure 2**a,b, respectively. In Figure 2a, electron sharing (connected isosurfaces) can be clearly observed between Cu12e–S2a, Cu12e–S24g, and Sb–S24g pairs, while there is limited sharing between Cu12e and Sb atoms. The "crescent-moon" shape around Sb is a clear indicator of the existence of electron lone pairs. The electron sharing can be better visualized by the ELF map in Figure 2b. First, the ELF function of Sb lone pairs is in the "bean" shape. Second, electrons between Cu12e and S24g are localized close to the S24g atoms, as expected from the larger Pauling electronegativity value of S (2.5) compared with Cu (1.9).[16] Between Cu12e and S2a pairs, electrons are localized toward the S2a atoms, with a smaller ELF value compared with Cu12e–S24 pairs. Similarly, electron localization between Sb and S24g atoms can be observed. Since the Pauling electronegativity of S is larger than that of Sb (1.9), the electron is localized at the S side. In addition to 2D maps, ELF functions can also be examined in 3D to gain a spatial perspective. For example, the "bean"-shaped Sb lone pairs behave as a "mushroom" surrounded by three Cu12e atoms, as shown in Figure 2c. On the other hand, the electron localization between Sb—S24g bonds in Figure 2c and Cu12d—S24g bonds in Figure 2d resembles a "dried-mushroom."

In addition to 2D and 3D maps, electron charge density can be quantified as atomic charges around atoms and bond orders between atom pairs, as shown in Table S3 (Supporting Information). Two types of atomic charges, i.e., Bader and density derived electrostatic and chemical charge (DDEC), are employed in the present study. The Bader charge method assigns atomic regions according to zero flux surfaces of the 3D charge density.[17] DDEC charges are derived from fitting the electrostatic potential and could reflect the real charge relevant to Coulombic interaction.[18] As expected, these two different methods lead to different values of charges. In the following discussion, we will focus on the DDEC charge method together with DDEC bond orders but discussion results will not change if we use the Bader charge method. First, we noticed that all atomic charges deviate significantly from their formal values, suggesting predominantly covalent bonding. Second, the observation that Cu12d has a higher positive charge (0.43) than Cu12e (0.35) suggests that Cu12d is slightly more ionic than Cu12e. This is supported by the lower bond order of Cu12d—S24g (0.61) compared with Cu12e—S24g (0.77). The bonding between Sb and S24g is mainly covalent with a high bond order of 0.95. Interestingly, a bond order of 0.10 was detected between Cu12e and out-of-plane Sb atoms.

2.3. Local Structure

Both the "average0" and "average1" structures are from crystallographic studies. If we relax the atoms in the "average0" structure and perform DFT-based energy minimization, atoms will be displaced and we name the resulting structure as "local0." The structure and bonding in "local0," shown in Table S3 (Supporting Information), is similar to that in "average0," except that the bond order of Cu12e–S2a (0.67) is smaller than Cu12e–S24g (0.79) in "local0," while the opposite was observed in "average0." In "average0," each Sb atom is connected to three Cu12e atoms with a length of 3.402 Å. From the following discussion of FPMD results, the Cu12e–Sb distance can vary from 2.5 to 4.3 Å. We will designate the representative frames in the atomic trajectory of FPMD simulation as "localx." For example, we selected one snapshot from the trajectory (hereafter named "local1") for which one Sb atom, named Sb1, has one long bond (3.928 Å), one medium bond (3.265 Å), and one short bond (2.771 Å). In addition, we selected another snapshot (hereafter named "local2") for which one Sb atom, also named Sb1, has three short bonds (2.776, 2.828, and 2.863 Å).

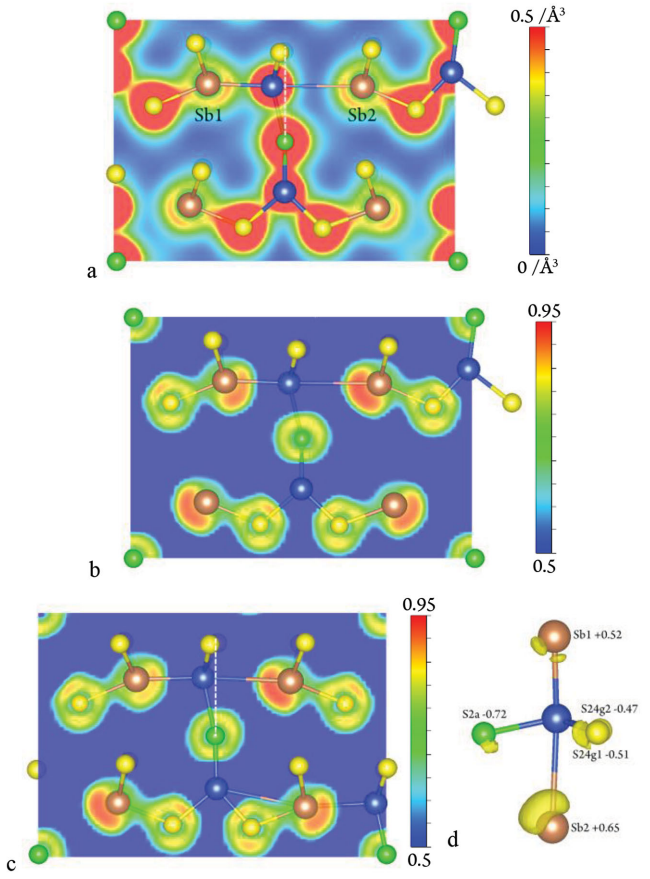

Figure 3. Valence electron density and ELF maps of the a,b) "local1" and c,d) "local2" structures. a) Valence electron density map of the "local1" structure projected onto a (101) plane showing the coordination of Cu12e, Sb, S2a, and S24g atoms. The dashed line represents the triangular plane. b) ELF map of the same atoms as in (a). c) ELF map of the "local2" structure projected onto a (101) plane. d) ELF maps of a $Sb[CuS_3]Sb$ trigonal bipyramid (isosurface level of 0.87) with DDEC atomic charges.

2.4. Valence Electron Charge Density and Bonding: Local1 and Local2

Charge density and ELF maps of the "local1" snapshot are shown in **Figure 3**a,b. This snapshot captures the out-of-plane (plane shown as the dashed line in Figure 3a) motion of one Cu12e atom, with a distance between Cu12e and the closer Sb1 atom of 2.771 Å. The farther Sb2 atom has three distances to Cu12e (3.234, 3.516, and 3.891 Å) with 3.891 Å shown in Figure 3a. While limited electron sharing is observed between Cu12e and two Sb atoms in Figure 2a, much stronger sharing is visible between Cu12e and the closer Sb1. The bond order of Cu12e–Sb1 pair is 0.35, indicating significant increase of covalent bonding. On the other hand, there is almost no electron sharing between Cu12e–Sb2 with a bond order of 0.04. At the same time, the DDEC charges of Sb1 and Sb2 atoms are 0.577 and 0.618, respectively. This suggests that the motion of Cu12e atom strongly modulates the electron density distribution in the material. The ELF map reveals that the localization region of the bonding Sb1 atom is smaller than that of the nonbonding Sb2 atom on the other side of the plane. This is apparently caused by the increased covalent bonding between Sb1 and Cu12e, while all three Cu12e–Sb2 distances can be considered as nonbonding, similar to that in Figure 2b.

The ELF map of the "local2" snapshot is shown in Figure 3c. The distance between Sb1 and Cu12e on the projection plane is 2.828 Å with a bond order of 0.30. The distance between Sb2 and Cu12e on the map is 3.709 Å with a bond order of 0.05. These values are similar to those in "local1" snapshot. The ELF region around Sb1 exhibits features closer to covalent bonding instead of lone pairs. This can be better visualized in the 3D space in Figure 3d. While the "mushroom" shape of electron lone pairs persists for the nonbonding Sb2 atom, the lone pairs of the bonding Sb1 atom separate into three "dried-mushroom" regions, similar to other covalent bonding configurations between Sb and S. From the comparison of ELF maps of covalent electron "pairs" and lone electron pairs, it can be seen that the covalent electrons are more localized with intermediate high ELF values, while lone pairs are more delocalized with very high ELF values. The DDEC charges are also shown Figure 3d. The charge of Sb1 is lower than that of Sb2 since it has three short Cu12e–Sb pairs with significant amount of covalent bonding.

2.5. Bond Order versus Bond Distance

To focus on the bonding environment in the $Sb[CuS_3]Sb$ trigonal bipyramids, we compiled the bond order values of Cu12e–Sb, Cu12e–S2a, and Cu12e–S24g pairs from selected "localx" structures; the results are plotted in **Figure 4** as a function of the bond distance (BD). Each dataset can be fitted to an exponential dependence as $BO = a \cdot \exp(-BD/b)$. In addition, we also compiled the bond distances of the three pairs from the FPMD trajectory and plotted the average values and standard deviation in Figure 4. All three bonds have average values very similar to those in the "local0" structure (Table S1, Supporting Information), suggesting that "local0" is able to capture ensemble average of the dynamics. The average bond order of

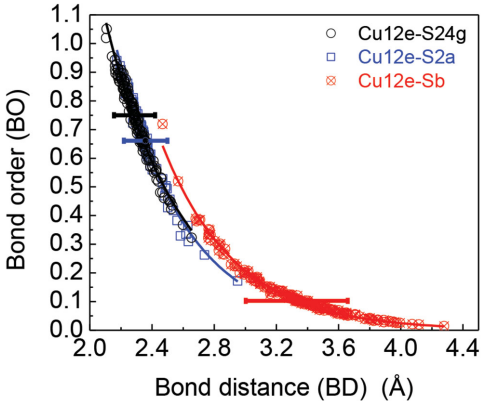

Figure 4. Plot of bond order as a function of bond distance of pairs within $Sb[CuS_3]Sb$ trigonal bipyramids. The solid lines represent the fit to the equation $BO = a \cdot \exp(-BD/b)$ with a and b values: Cu12e–S2a (130.0, 0.44 Å), Cu12e–S24g (79.0, 0.49 Å), and Cu12e–Sb (122.1, 0.47 Å). The error bars represent the standard deviation of bond distances from the FPMD trajectory at 300 K.

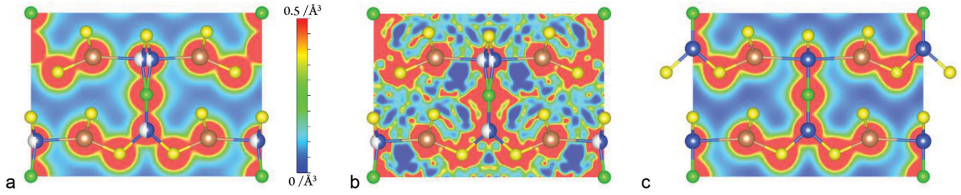

Figure 5. Total electron density maps on a (101) plane. a) Rietveld refinement of synchrotron diffraction data. b) Maximum entropy method analysis of synchrotron diffraction data and c) DFT calculation of the "average0" structure.

Cu12e–S24g (0.75) is higher than that of Cu12e–S2a (0.66), consistent with values from the "local0" structure. The out-of-plane bond pairs Cu12e–Sb have an average bond order of 0.10. We believe such bonding asymmetry is closely related to the anharmonicity to be discussed shortly.

2.6. Total Electron Charge Density

X-ray diffraction probes the total, rather than the valence, electron density distribution in the material. Total electron charge density maps from the Rietveld refinement (a) and maximum entropy method (MEM) analysis of diffraction data (b), and DFT-based energy minimization (c) are shown in **Figure 5**. First, the information on the location and shape of lone electron pairs of Sb is missing from the total electron density map in Figure 5c, even by choosing different contour ranges. Second, electron sharing between covalent bonding of Sb—S and Cu—S can be identified in the map from the Rietveld refinement in Figure 5a. However, a close inspection indicates that the electron sharing is not as strong as in Figure 5c. This can be understood from the assumption of the Rietveld refinement employed in the present study: independent and harmonic motion with spherical electron density. This will only yield a 3D Gaussian distribution around each atom and cannot treat the electron sharing in covalent bonding intrinsically. However, overlapping of the Gaussian tails between neighboring atoms will lead to increased local electron density that resembles covalent bonding. Thus it is still feasible to study covalent bonding based on the Rietveld refinement. The MEM analysis reconstructs the total electron density by maximizing the information entropy that depends on the electron density.[19] Results from the Rietveld refinement were used as the constraint in the MEM analysis. However, there is no independent, harmonic, or spherical requirement. As expected, the electron density from the MEM analysis is highly anharmonic and delocalized in Figure 5b, in which the electron sharing within covalent bonds can be clearly identified.

2.7. Vibrational Density of States and Atomic Displacement

Armed with this new knowledge of the chemical bonding, we now examine the dynamic behaviors to correlate the chemical bonding and atomic dynamics. First, the temperature dependence of lattice parameters from the FPMD simulation and diffraction experiments are comparable (Figure S1, Supporting Information). Second, the VDOS of all atoms are shown in **Figure 6** for both 300 and 600 K. Broadly speaking, there are two groups of peaks: one group of low-lying modes (0–25 meV) and the other group of high-energy modes (25–60 meV). Similar separation of low- and high-energy modes was observed in a lattice dynamical study of $Cu_{12}Sb_4S_{13}$, along with negative energy modes.[7a] In Figure 6a, high-energy modes are mainly attributed to S atoms, while all atoms contribute to the low-lying modes. The lower-end of these low-lying modes (<5 meV) exhibits a peak marked by the dashed line at around 4 meV (equivalent to 48 K, 1 THz, or 33 cm^{-1}). We call these modes as quasilocalized since they are predominately associated a subset of atoms in the material, i.e., Cu12e. These modes signify weak bonding due to their low frequencies and low energies.[20] In addition, they can also be considered as large-amplitude vibration modes since the frequency/energy is inversely proportional to amplitude. In a similar compound Cu_3SbSe_3 also containing two groups of Cu atoms (Cu1 and Cu2), the vibrations of Cu1 and Cu2 are closely coupled with no quasilocalized modes.[20b]

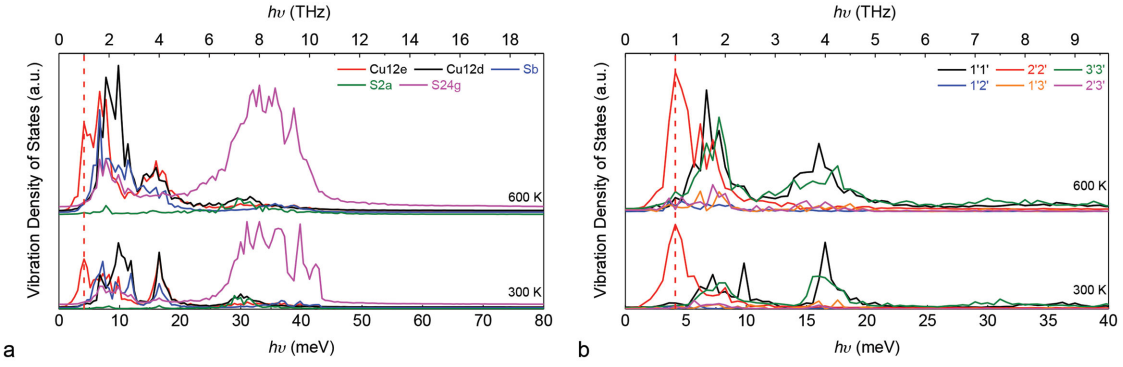

Figure 6. Vibration density of states in $Cu_{12}Sb_4S_{13}$ tetrahedrites at 300 and 600 K. a) Isotropic motion of all atoms. b) Anisotropic motion of Cu12e atoms. The dashed line indicates the vibration peak at ≈4 meV.

In Figure 6a, the higher end of low-lying modes of Cu12e (5–20 meV) are less localized. For example, atoms of Cu12e, Sb, Cu12d, and S24g all exhibit a peak at around 7.5 meV in Figure 6a, suggesting that vibration of Cu12e in this energy range is globally coupled to that of other atoms. Similar low energy modes were observed in $Yb_{0.2}Co_4Sb_{12}$ skutterudite for Yb atom[21] and in $Ba_8Ga_{16}Ge_{30}$ clathrate for Ba atom at ≈5 meV.[22] A recent study of $Cu_{10}Zn_2Sb_4S_{13}$ found that three Einstein modes at ≈1.0, 2.8, and 8.4 meV are required to describe the low-temperature heat capacity from a combined Debye/Einstein model.[23] As the temperature is increased to 600 K, the fraction of the higher energy region in the low-lying modes increases.

To correlate the "rattling" modes with atomic motion, we further plotted the anisotropic VDOS of Cu12e in Figure 6b. Clearly the "rattling" modes are due to the Cu12e vibration along the 2′2′ direction, which is the out-of-plane vibration shown in Figure 1b. The out-of-plane "rattling" modes are also correlated with an out-of-plane displacement. We analyzed the atomic trajectory at 300 K to obtain a distribution of distance of Cu12e to the triangular plane, shown in Figure S2 (Supporting Information). A large fraction of Cu12e atoms actually sit at or close to in-plane positions, although the out-of-plane distance can be as large as 0.8 Å. The average distance is 0.27 Å with a standard deviation of 0.18 Å. This value of 0.27 Å is very close to 0.30 Å in the "average1" structure, which could indicate the advantage of the split-site over anisotropic model. It is also close to 0.32 Å from the lattice dynamic study.[7a]

In the time domain, crystallographic ADPs (U) can be obtained from the mean square displacement analysis of the FPMD trajectory. These values, labeled as "MSD," are shown in **Figure 7**, along with those from the Rietveld refinement. The standard Rietveld refinement method treats each ADP parameter as an independent harmonic oscillator with a single frequency. For example, the anisotropic ADP of $U_{2'2'}$ of Cu12e being 0.1431 Å^2 at 300 K (Table S1, Supporting Information) corresponds to a delta peak at 3.45 meV in the VDOS plot in Figure 6b. The difference between "MSD" and "RR" plots in Figure 7 is thus likely caused by the atomic correlation or anharmonic effects. Furthermore, $U_{2'2'}$ values of Cu12e from the "MSD" approach start to reach a plateau (corresponding to displacement of 0.35 Å) as the temperature increases. This suggests that the increase in size of the Sb[CuS_3]Sb trigonal bipyramid lags behind the increase in amplitude of Cu12e, causing a confined cage for its out-of-plane motion.

According to the Lindemann criterion of melting,[24] the ADP parameter is related to the Lindemann melting parameter δ as $\delta = \mathrm{ADP}^{1/2}/R_{NN}$, where R_{NN} is the nearest-neighbor distance. The large ADP value of $U_{2'2'}$ = 0.1431 Å^2 of Cu12e atoms and a 3.2 Å of R_{NN} yield a δ parameter of 0.12, exceeding the melting threshold value of 0.07. A much larger Lindemann parameter of 0.44 for two types of Cu atoms was observed in a similar compound Cu_3SbSe_3, leading to part-crystalline and part-liquid structure.[20b] However, neither the time dependence of MSD, the frequency dependence of VDOS, or the atomic p.d.f. to be discussed shortly exhibits diffusive dynamics in $Cu_{12}Sb_4S_{13}$ tetrahedrites up to 600 K. Thus we characterize $Cu_{12}Sb_4S_{13}$ tetrahedrites as part-crystalline and part-glassy instead.

2.8. Anharmonicity: Atomic p.d.f.

Just as the valence/total electron charge density can be employed to understand the electronic structure discussed previously, nuclear density, also called number density or atomic p.d.f., can be utilized to investigate the time-averaged atomic dynamics. If the atomic motion is independent and harmonic, as assumed in the Rietveld refinement, the nuclear density is a 3D Gaussian function and nuclear density isosurface shape should be either spherical (isotropic) or ellipsoidal (anisotropic). The nuclear density maps of all atoms in $Cu_{12}Sb_4S_{13}$ tetrahedrite at 300 K are shown in **Figure 8**. 3D maps viewed along [111] directions are shown in (a–e), with an isosurface level of 0.5 Å^{-3}. It is to be noted that the isosurface in Figure 1b corresponds to the surface within which the integration of p.d.f., i.e., probability, is 90%. In Figure 8, it can be seen that the motion of Cu12d, Sb, S2a, and S24g atoms is close to being harmonic, considering the spheroid shape. However, the motion of Cu12e is highly anharmonic. While there is clearly elongation across the triangular plane, the shape of isosurface is not close to being ellipsoid. To better visualize the anharmonicity, nuclear density maps are projected onto a (101) plane where different isosurface levels are visible. As expected, the density maps are harmonic for data from the Rietveld refinement, i.e., Figure 8f. The slight deviation from a circle or ellipse is due to the finite pixel resolution (0.1 Å along each direction).

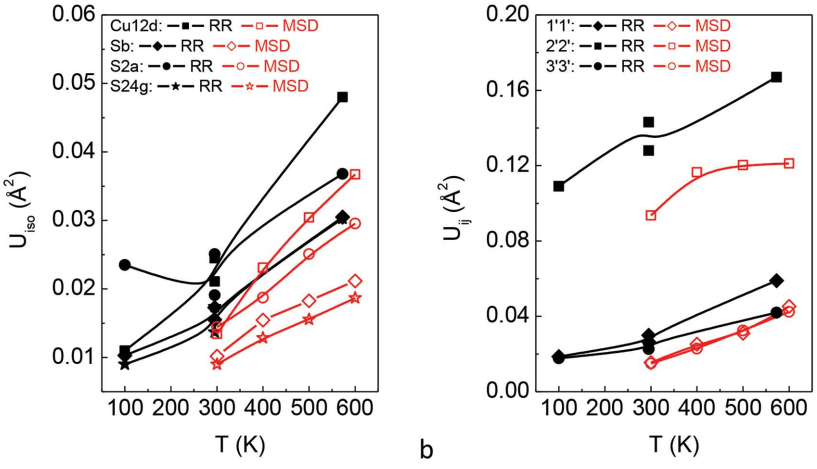

Figure 7. Isotropic/anisotropic atomic displacement parameters of $Cu_{12}Sb_4S_{13}$ tetrahedrites at different temperatures. Solid lines are guides to the eye. a) Isotropic atomic displacement parameters of all atoms. Values from the Rietveld refinement of synchrotron diffraction experiments in this work and from Pfitzner et al.[13] are labeled as "RR." Values from the analysis of mean square displacement (MSD) of the FPMD trajectory are labeled as "MSD." The crystallographic U values are half of the corresponding MSD values. b) Anisotropic atomic displacement parameters of Cu12e atoms in the local coordination system.

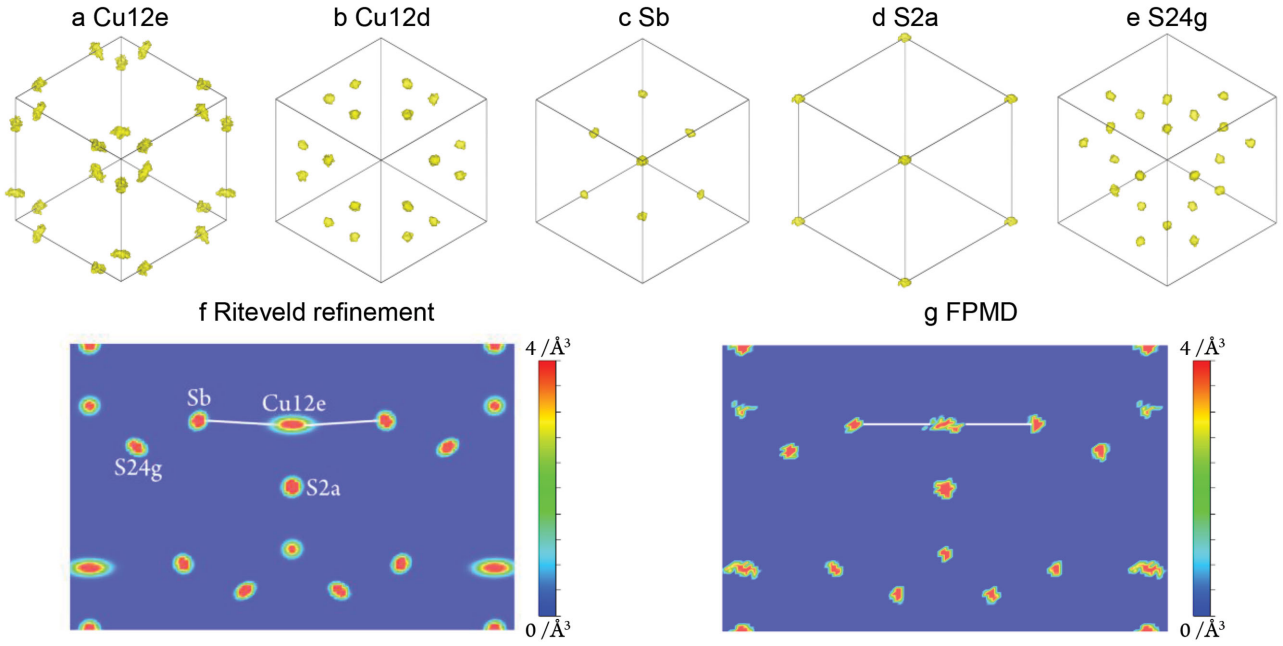

Figure 8. Nuclear density maps at 300 K. 3D nuclear density maps from the FPMD of atoms a) Cu12e, b) Cu12d, c) Sb, d) S2a, and e) S24g viewed along [111] direction, with an isosurface level is 0.5 Å^{-3}. f) 2D projection onto a (101) plane for Rietveld refinement results. g) 2D projection onto a (101) plane for FPMD results.

As shown earlier in Figure 1b, the angle of Sb–Cu12e–Sb triplet is ≈175°, while FPMD results suggest a linear connection.

To further quantify the magnitude of the deviation from a Gaussian function for the Cu12e atom, the line profiles of atomic p.d.f. and one-particle potentials (O.P.P.) along the Sb–Cu12e–Sb directions are shown in **Figure 9**a. Two different Sb–Cu12e–Sb triplets, called Directions 1 and 2, are presented. The atomic p.d.f. of Cu12e has multiple peaks instead taking a single Gaussian shape. These peaks convert to three visible local minima in the O.P.P. plot. If we use the split-site model, i.e., "average1," there are two out-of-plane positions at ≈0.30 Å with a double-well potential, consistent with the lattice dynamic study of Lu et al.[7a] The overall shape of O.P.P. of the two directions and the split-site model can be fit with a quartic polynomial as shown in Figure 9a, which suggests the overall potential surface is fourth-order anharmonic. Such a quartic potential was also reported in $X_8Ga_{16}Ge_{30}$ clathrate (X = Eu, Sr, Ba) studied by Raman scattering.[25] Examination of O.P.P. of other atoms suggests that their potential can be fit into either a harmonic or a quartic potential with a quartic potential giving a slightly better fit.

We can apply the similar concept to the bond distance. First we obtain the probability density functions of bond distances of Cu12e–S24g, Cu12e–S2a, and Cu12e–Sb pairs from the FPMD trajectory. Then we convert them to effective one-pair-potentials (O.Pr.P.) as shown in Figure 9b. The potentials between Cu12e and S2a/S24g depend on the bond distances in a fashion typical of asymmetrical anharmonicity, e.g., a Morse function.

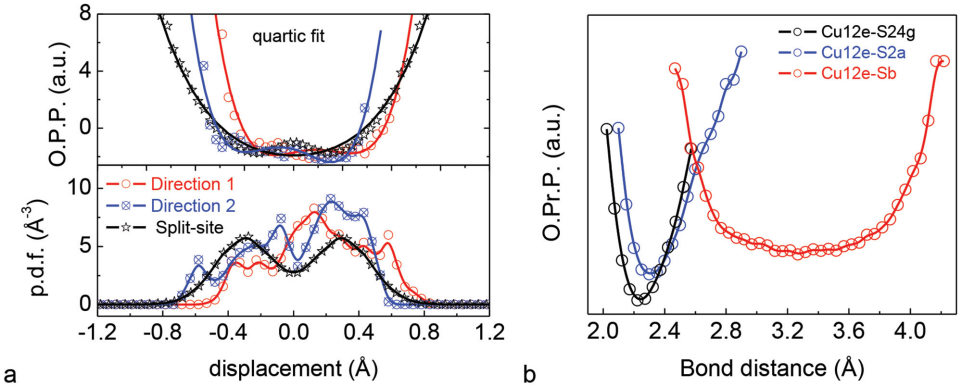

Figure 9. Atomic p.d.f. and effective potentials depicting the anharmonicity. a) 1D line profiles of atomic p.d.f. and one-particle-potential (O.P.P.) values along Sb–Cu12e–Sb triplets. Directions 1 and 2 and two different Sb–Cu12e–Sb triplets. Results from the split-site model, i.e., "average1," are also shown for comparison. In the p.d.f. plot, solid lines are guides to the eye. In the O.P.P. plot, solid lines are quartic fit. b) Bond distance p.d.f. and O.Pr.P. values of Cu12e–S24g, Cu12e–S2a, and Cu12e–Sb pairs. Solid lines are guides to the eye.

The potential of Cu12e–Sb pair is close to being symmetric of a fourth-order polynomial. Its flat bottom implies that large change of bond distance can be accommodated without much energy penalty, which drives the low-frequency/large-amplitude vibration modes.

2.9. Bonding Fluctuation

As discussed previously, the bond length is closely related to the bond order. In order to study how the bonding of three Cu12e–Sb pairs changes around Sb atom, we plotted the variation of bond lengths as a function of simulation time in **Figure 10**. First, it can be noticed that the bond length of each Cu12e–Sb pair oscillates around an equilibrium value (3.339, 3.293, and 3.316 Å), i.e., bottom panel of Figure 10. The equilibrium value corresponds to Cu12e being located in the middle of two Sb atoms. Then we assigned a value of 1 (bonding) and 0 (non-bonding) to the bond length below and above the equilibrium value, respectively. Finally, we will add bond values from three bonds together as a single indicator of the bonding of Cu12e to this Sb atom. This indicator, called bond number, is also shown in the top panel of Figure 10. The bond number of Sb atom varies from 0 to 3, with an average value close to 1.5. A value of 3 corresponds to three short pairs and a value of 0 corresponds to three long pairs. The bond number values of 1 and 2 are frequently observed.

For each Sb atom, we have more bonding configurations (3) than the actual number of bonds (1.5). Focusing on the Cu12e atom, there are two bonding configurations to Sb on either side of the triangular plane but only one Cu12e—Sb bond exists at any time. We will call such a phenomenon as bonding fluctuation. A similar example is the resonant/resonance bonding in benzene. The argument is that six, instead of 12, electrons are shared among six C—C bonds. Alternatively, this means there are six bonding configurations but the actual number of "bond pairs" (each bond pair has exactly two electrons) is only three. In solids, a hypothetical Sb solid was used as an example, in which three *p* electrons of each Sb atom form six bonds.[26] In these literatures, the concept of resonance is associated with electron delocalization. In the present discussion of $Cu_{12}Sb_4S_{13}$ tetrahedrites, the bonding fluctuation is associated with the slower atomic delocalization of Cu12e, which is driven by its interaction with the electron lone pair of Sb atom.

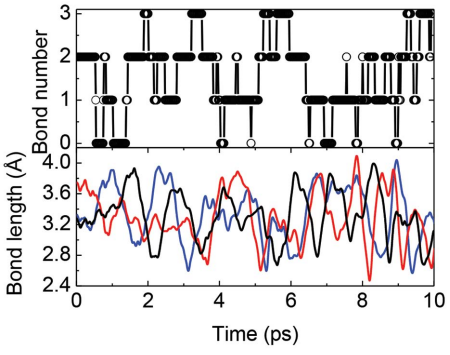

Figure 10. Bond length values (bottom panel) of three Cu12e–Sb atomic pairs (black, red, and blue) and the overall bond number (top panel) around one Sb atom.

3. Discussion and Conclusion

In this work, we studied the chemical bonding and atomic dynamics of a prototypical tetrahedrite $Cu_{12}Sb_4S_{13}$ or $(Cu12d)_{12}(Cu12e)_{12}(Sb8c)_8(S2a)_2(S24g)_{24}$, with a combination of first-principles simulation and synchrotron diffraction experiments. Results from the simulation are largely consistent with those from experiments, which allows us to gain deeper insight into the atomic and electronic structure and dynamics of the material.

We believe that the unique structural and bonding characteristic in $Cu_{12}Sb_4S_{13}$ is the interaction of Cu12e with electron lone pairs of Sb. This effectively modifies the CuS_3, i.e., (Cu12e)(S2a)$(S24g)_2$, trigonal planes to Sb[(Cu12e)S_3]Sb trigonal bipyramids, thus creating the oversized, although only five-atom, atomic cage that is required in the context of PGEC and rattlers. Inside this cage, Cu12e forms a triangular plane with two S24g atoms and one S2a atom, with strong (bond order ≈ 0.75) and intermediately strong (bond order ≈ 0.66) covalent bonding to S24g and S2a, respectively. Along the out-of-plane direction, a weak (bond order ≈ 0.10) bonding configuration exists between Cu12e and one of the Sb atoms (bonding fluctuation) that varies from lone pair to covalent bonding. In the meantime, the lone-pair electrons also effectively modify the SbS_3 trigonal pyramids to S_3SbCu_3 trigonal antiprisms with bonding fluctuation at the Sb site.

We believe such strong local bonding asymmetry is the origin of anharmonic rattling. The bonding fluctuation at Cu12e site enabled by lone-pair electrons adds perturbations to the potential energy surface and naturally leads to a symmetric but flat (anharmonic) potential. This flat potential surface induces quasilocalized rattling modes with low frequency and large amplitude. These vibration modes are mainly along the out-of-plane direction with an energy or frequency value of ≈4 meV, 48 K, 1 THz, or 33 cm^{-1}. In a recent study on Cu_3SbSe_3, a link was presented between the chemical-bond hierarchy (i.e., bonding asymmetry), part-crystalline/part-liquid state, and rattling behaviors.[20b] However, the origin of bond hierarchy, especially the role of lone-pair atom (Sb), was not discussed. We expect that lone-pair electrons of Sb will have a similar influence in Cu_3SbSe_3 considering the similar crystal structure of these two compounds.

The correlation of local structure, bonding asymmetry, and rattling behavior was also observed in ionic conductors with predominantly ionic bonding. For example, a characteristic cluster in lithium garnet oxides $Li_5La_3Ta_2O_{12}$ is (Li24d)[(Li48g)O_6](Li24d) in which Li24d and Li48g sit inside a tetrahedral and octahedral cage, respectively.[27] This cluster can be considered as the oversized atomic cage analogous to Sb[(Cu12e)S_3]Sb trigonal bipyramids in tetrahedrites. The center of the cage (48g site) is characterized by two short, two intermediate, and two long Li–O distances. This asymmetry intrinsically drives the on-center Li atom to move off-center, favoring a four coordination. Furthermore, Li48g in the octahedral cage can be repelled by the neighboring Li24d atoms due to their close proximity (≈2

Å). The two tetrahedral Li atoms are analogous to Sb atoms in tetrahedrites and can take the occupancy pattern of (0 0), (1 1), or (0 1). This dynamic and asymmetrical bonding environment causes the rattling motion of Li at the 48g site. Since the octahedral and tetrahedral cages in lithium garnet oxides are continuously connected, the rattling mode propagates through all the cages, converting rattlers to diffusing atoms and ionic conduction. These materials exhibit the classical part-crystalline and part-liquid structure and dynamics.[27b]

In the context of thermoelectric performance, we believe that the anharmonic rattling mode in tetrahedrites is the reason for low thermal conductivity. One of the hypotheses is based on the concept of "avoided crossing,"[28] in which the localized vibration mode flattens the heat-carrying acoustic phonon branch. In $Cu_{12}Sb_4S_{13}$, it means that the acoustic phonon branch is suppressed to below 4 meV by the out-of-plane motion of Cu12e. This reduces the mean sound velocity and contributes to the low thermal conductivity. In addition, localized rattling modes can contribute to resonant scattering of phonons,[21] which can be considered as a different flavor of "avoided crossing."[29] The present work suggests that we can look for compounds that host local structure asymmetry (to provide bonding asymmetry) and lone pair atoms (to provide bonding asymmetry and rattling modes), in order to search for thermoelectric materials with minimum thermal conductivity. This provides a stepping stone to the discovery and design of next-generation thermoelectrics.

4. Experimental Section

Materials Synthesis: Stoichiometric quantities of high purity raw elements—copper pellets (99.999% Alfa Aesar), antimony shot (99.999% Alfa Aesar), and sulfur chunks (99.999%, Alfa Aesar)—were loaded into a quartz ampoule and evacuated to 10^{-5} Torr. The ampoule was subsequently sealed, suspended in a vertical furnace, heated at a rate of 0.3 °C min^{-1} to 700 °C, and soaked for 12 h. The furnace was then cooled to room temperature at the rate of 0.4 °C min^{-1}. In order to obtain homogeneous single phase tetrahedrite, the resulting ingot was ground into powder and cold pressed into a pellet, which was reampouled under vacuum and heat treated for one week at 450 °C. The final product was pulverized into fine powders by hand using agate mortar and pestle.

Synchrotron Diffraction and Data Analysis: Synchrotron X-ray diffraction data of $Cu_{12}Sb_4S_{13}$ powders were collected at the 11-BM beamline (100 and 295 K) at the Advanced Photon Source of the Argonne National Laboratory. The wavelength of synchrotron radiation was 0.459004 Å. The Rietveld refinement and maximum entropy method analysis were performed using Jana2006[30] and Dysnomia,[31] respectively.

First-Principles Calculation and Data Analysis: DFT-based atomistic simulations were performed with the Projector Augmented Wave method[32] implemented in the Vienna Ab initio Simulation Package (VASP) package. Generalized gradient approximation of Perdew–Burke–Ernzerhof parametrization[33] was used for the exchange-correlation functional. Valence electron configurations for Cu, Sb, and S atoms are $3p^6 4s^1 3d^{10}$, $5s^2 5p^3$, and $3s^2 3p^4$, respectively. The simulation cell was $1 \times 1 \times 1$ supercell with 58 atoms. The plane-wave cutoff energy was 450 eV with a Gamma point for MD simulation and $3 \times 3 \times 3$ Monkhorst–Pack *k*-point meshes for static calculation. Constant number, pressure, and temperature simulations were performed with a Langevin thermostat and Parrinello–Rahman barostat to obtain lattice parameters at different temperatures. Then constant number, volume, energy simulations were performed with 2 ps for equilibration and 10 ps for sampling atomic trajectories. The time step of MD simulation was 1 fs. Atomic charges based on the Bader charge scheme[17] and DDEC scheme[18] were obtained from the Bader charge analysis code[34] and DDEC code,[18] respectively. The effective bond orders between atomic pairs were calculated from the DDEC code. ELF maps were produced intrinsically in VASP. We calculated the time-averaged number density of atom species *i* as $\rho_i(r)$, also called atomic p.d.f. or nuclear density, using the same approach as in the literature.[27b] Briefly, we first divided the simulation cell into cubic pixels with roughly 0.1 Å in length. Then we recorded whether each pixel was occupied by an atomic species, e.g., Cu or Sb, at each time step. Finally we averaged over all time steps to obtain the probability and then probability density. The one-particle-potential (O.P.P.) is related to the atomic p.d.f. as $-k_B T \ln \rho_i(r)$. Atomic MSDs were calculated according to the standard definition $\left\langle \left|\delta r_i(t)\right|^2 \right\rangle = 1/N_i \sum_{j=1}^{N_i} \left\langle \left| r_{i,j}(t) - r_{i,j}(0) \right|^2 \right\rangle$, where $r_{i,j}$ is the position of *j*th atom in atomic species *i* and N_i is the number of atoms of species *i*. VDOS were calculated from the Fourier transform of the mass-weighted velocity autocorrelation function,[35] with a Hanning window function to reduce truncation errors.[36] 3D isosurface, 2D contour, and 1D line profile plots were drawn with the VESTA program.[37]

Supporting Information

Supporting Information is available from the Wiley Online Library or from the author.

Acknowledgements

Use of the Advanced Photon Source at Argonne National Laboratory was supported by the U. S. Department of Energy, Office of Science, Office of Basic Energy Sciences, under Contract No. DE-AC02-06CH11357. The authors wish to acknowledge the Michigan State University High Performance Computing Center and the Institute for Cyber-Enabled Research for access to their computing resources. This work was supported as part of the Center for Revolutionary Materials for Solid State Energy Conversion, an Energy Frontier Research Center funded by the U.S. Department of Energy, Office of Science, Office of Basic Energy Sciences under Award Number DE-SC0001054.

Received: February 25, 2015
Revised: April 7, 2015
Published online: May 12, 2015

[1] G. J. Snyder, E. S. Toberer, *Nat. Mater.* **2008**, *7*, 105.
[2] a) G. A. Slack, in *CRC Handbook of Thermoelectrics* (Ed: D. M. Row), CRC Press, Boca Raton, FL **1995**; b) C. B. Vining, *Nat. Mater.* **2008**, *7*, 765.
[3] G. A. Slack, V. G. Tsoukala, *J. Appl. Phys.* **1994**, *76*, 1665.
[4] M. Christensen, B. B. Iversen, *Chem. Mater.* **2007**, *19*, 4896.
[5] C. Uher, *Recent Trends Thermoelectr. Mater. Res.* **2001**, *69*, 139.
[6] X. Lu, D. T. Morelli, Y. Xia, V. Ozolins, *Chem. Mater.* **2015**, *27*, 408.
[7] a) X. Lu, D. T. Morelli, Y. Xia, F. Zhou, V. Ozolins, H. Chi, X. Zhou, C. Uher, *Adv. Energy Mater.* **2013**, *3*, 342; b) K. Suekuni, K. Tsuruta, M. Kunii, H. Nishiate, E. Nishibori, S. Maki, M. Ohta, A. Yamamoto, M. Koyano, *J. Appl. Phys.* **2013**, 113; c) J. Heo, G. Laurita, S. Muir, M. A. Subramanian, D. A. Keszler, *Chem. Mater.* **2014**, *26*, 2047.
[8] G. A. Slack, in *Solid State Physics*, Vol. *34* (Eds: F. Seitz, D. Turnbull), Academic, New York **1979**.
[9] B. J. Wuensch, *Z. Kristallogr.* **1964**, *119*, 437.
[10] E. J. Skoug, D. T. Morelli, *Phys. Rev. Lett.* **2011**, *107*, 5.
[11] A. Walsh, G. W. Watson, *J. Solid State Chem.* **2005**, *178*, 1422.

[12] a) A. D. Becke, K. E. Edgecombe, *J. Chem. Phys.* **1990**, *92*, 5397; b) B. Silvi, A. Savin, *Nature* **1994**, *371*, 683; c) A. Savin, B. Silvi, F. Colonna, *Can. J. Chem.* **1996**, *74*, 1088.
[13] A. Pfitzner, M. Evain, V. Petricek, *Acta Crystallogr., Sect. B: Struct. Sci.* **1997**, *53*, 337.
[14] Y. X. Wang, A. Huq, W. Lai, *Solid State Ionics* **2014**, *255*, 39.
[15] B. C. Chakoumakos, B. C. Sales, D. G. Mandrus, G. S. Nolas, *J. Alloys Compd.* **2000**, *296*, 80.
[16] W. D. Callister, D. G. Rethwisch, *Materials Science and Engineering: An Introduction*, John Wiley & Sons, Inc, New York, NY **2009**.
[17] R. F. W. Bader, *Atoms in Molecules - A quantum theory*, Oxford University Press, New York, NY **1990**.
[18] T. A. Manz, D. S. Sholl, *J. Chem. Theory Comput.* **2012**, *8*, 2844.
[19] a) D. M. Collins, *Nature* **1982**, *298*, 49; b) M. Sakata, M. Sato, *Acta Crystallogr., Sect. A: Found. Crystallogr.* **1990**, *46*, 263.
[20] a) V. Keppens, D. Mandrus, B. C. Sales, B. C. Chakoumakos, P. Dai, R. Coldea, M. B. Maple, D. A. Gajewski, E. J. Freeman, S. Bennington, *Nature* **1998**, *395*, 876; b) W. Qiu, L. Xi, P. Wei, X. Ke, J. Yang, W. Zhang, *Proc. Natl. Acad. Sci. U.S.A.* **2014**, *111*, 15031.
[21] X. Shi, J. Yang, J. R. Salvador, M. F. Chi, J. Y. Cho, H. Wang, S. Q. Bai, J. H. Yang, W. Q. Zhang, L. D. Chen, *J. Am. Chem. Soc.* **2011**, *133*, 7837.
[22] M. Christensen, S. Johnsen, F. Juranyi, B. B. Iversen, *J. Appl. Phys.* **2009**, *105*, 9.
[23] E. Lara-Curzio, A. F. May, O. Delaire, M. A. McGuire, X. Lu, C. Y. Liu, E. D. Case, D. T. Morelli, *J. Appl. Phys.* **2014**, *115*, 6.
[24] F. A. Lindemann, *Phys. Z.* **1910**, *11*, 609.
[25] Y. Takasu, T. Hasegawa, N. Ogita, M. Udagawa, M. A. Avila, K. Suekuni, I. Ishii, T. Suzuki, T. Takabatake, *Phys. Rev. B* **2006**, *74*, 174303.
[26] a) K. Shportko, S. Kremers, M. Woda, D. Lencer, J. Robertson, M. Wuttig, *Nat. Mater.* **2008**, *7*, 653; b) S. Lee, K. Esfarjani, T. Luo, J. Zhou, Z. Tian, G. Chen, *Nat. Commun.* **2014**, *5*, 3525.
[27] a) E. J. Cussen, *J. Mater. Chem.* **2010**, *20*, 5167; b) Y. X. Wang, M. Klenk, K. Page, W. Lai, *Chem. Mater.* **2014**, *26*, 5613.
[28] a) M. Christensen, A. B. Abrahamsen, N. B. Christensen, F. Juranyi, N. H. Andersen, K. Lefmann, J. Andreasson, C. R. H. Bahl, B. B. Iversen, *Nat. Mater.* **2008**, *7*, 811; b) O. Delaire, J. Ma, K. Marty, A. F. May, M. A. McGuire, M. H. Du, D. J. Singh, A. Podlesnyak, G. Ehlers, M. D. Lumsden, B. C. Sales, *Nat. Mater.* **2011**, *10*, 614.
[29] a) J. Baumert, C. Gutt, V. P. Shpakov, J. S. Tse, M. Krisch, M. Muller, H. Requardt, D. D. Klug, S. Janssen, W. Press, *Phys. Rev. B* **2003**, *68*, 7; b) J. S. Tse, Z. Li, K. Uehara, *Europhys. Lett.* **2001**, *56*, 261.
[30] V. Petricek, M. Dusek, L. Palatinus, *Z. Kristallogr.* **2014**, *229*, 345.
[31] K. Momma, T. Ikeda, A. A. Belik, F. Izumi, *Powder Diffr.* **2013**, *28*, 184.
[32] a) G. Kresse, D. Joubert, *Phys. Rev. B* **1999**, *59*, 1758; b) P. E. Blochl, *Phys. Rev. B* **1994**, *50*, 17953.
[33] a) J. P. Perdew, K. Burke, M. Ernzerhof, *Phys. Rev. Lett.* **1997**, *78*, 1396; b) J. P. Perdew, K. Burke, M. Ernzerhof, *Phys. Rev. Lett.* **1996**, *77*, 3865.
[34] a) G. Henkelman, A. Arnaldsson, H. Jonsson, *Comput. Mater. Sci.* **2006**, *36*, 354; b) E. Sanville, S. D. Kenny, R. Smith, G. Henkelman, *J. Comput. Chem.* **2007**, *28*, 899; c) W. Tang, E. Sanville, G. Henkelman, *J. Phys.: Condens. Matter* **2009**, *21*, 084204.
[35] a) S. T. Lin, M. Blanco, W. A. Goddard, *J. Chem. Phys.* **2003**, *119*, 11792; b) M. T. Dove, *Introduction to Lattice Dynamics*, Cambridge University Press, New York, NY **1993**.
[36] F. J. Harris, *Proc. IEEE* **1978**, *66*, 51.
[37] a) K. Momma, F. Izumi, *J. Appl. Crystallogr.* **2008**, *41*, 653; b) K. Momma, F. Izumi, *J. Appl. Crystallogr.* **2011**, *44*, 1272.